ADVANCED MATERIALS
www.advmat.de

Improving Image-Guided Surgical and Immunological Tumor Treatment Efficacy by Photothermal and Photodynamic Therapies Based on a Multifunctional NIR AIEgen

Ruming Jiang, Jun Dai, Xiaoqi Dong, Quan Wang, Zijuan Meng, Jingjing Guo, Yongjiang Yu, Shixuan Wang, Fan Xia, Zujin Zhao, Xiaoding Lou,* and Ben Zhong Tang**

Multimodal therapy is attracting increasing attention to improve tumor treatment efficacy, but generally requires various complicated ingredients combined within one theranostic system to achieve multiple functions. Herein, a multifunctional theranostic nanoplatform based on a single aggregation-induced-emission luminogen (AIEgen), DDTB, is designed to integrate near-infrared (NIR) fluorescence, photothermal, photodynamic, and immunological effects. Intravenously injected AIEgen-based nanoparticles can efficiently accumulate in tumors with NIR fluorescence to provide preoperative diagnosis. Most of the tumors are excised under intraoperative fluorescence navigation, whereafter, some microscopic residual tumors are completely ablated by photodynamic and photothermal therapies for maximally killing the tumor cells and tissues. Up to 90% of the survival rate can be achieved by this synergistic image-guided surgery and photodynamic and photothermal therapies. Importantly, the nanoparticles-mediated photothermal/photodynamic therapy plus programmed death-ligand 1 antibody significantly induce tumor elimination by enhancing the effect of immunotherapy. This theranostic strategy on the basis of a single AIEgen significantly improves the survival of cancer mice with maximized therapeutic outcomes, and holds great promise for clinical cancer treatment.

1. Introduction

Cancer kills millions of people every year, and has become a serious threat to the health of human beings.[1] Currently, surgery is the most widely used curative treatment in clinical for the patients with solid tumors.[2] Although surgical treatment can effectively remove tumor masses visible to the naked eye by surgeon, some tiny tumors are often missed and left behind after operation, which could lead to the treatment failure for patients on account of the residual lesion and cancer recurrence.[3] Therefore, the development of effective cancer treatment strategy for obtaining desirable therapeutic outcome is an urgent demand, yet a significantly challenging task.

As a rising star, phototheranostics has attracted widespread attention in recent years for cancer treatment, which allows for diagnosis and concurrent in situ therapy triggered by light.[4] Numerous protocols of diagnostic imaging and therapy have continuously sprung up for establishing phototheranostic systems to date.[5] Among various existing diagnostic imaging modalities, fluorescence imaging (FLI) has captivated much interest due to the significant advantages of fast response, excellent sensitivity, real-time monitor, and relatively low cost.[6] It should be mentioned that near-infrared (NIR) FLI holds merits of deep-tissue penetration and negligible autofluorescence and thus generally exhibits better performance than visible FLI.[7] Therefore, NIR FLI, especially NIR-II FLI, could

R. Jiang, J. Guo, Y. Yu, Prof. Z. Zhao, Prof. B. Z. Tang
State Key Laboratory of Luminescent Materials and Devices
Guangdong Provincial Key Laboratory of Luminescence from Molecular Aggregates
SCUT-HKUST Joint Research Institute
South China University of Technology
Guangzhou 510640, China
E-mail: mszjzhao@scut.edu.cn; tangbenz@ust.hk

Dr. J. Dai, Prof. S. Wang
Department of Obstetrics and Gynecology
Tongji Hospital
Tongji Medical College
Huazhong University of Science and Technology
Wuhan 430074, China

X. Dong, Q. Wang, Z. Meng, Prof. F. Xia, Prof. X. Lou
Engineering Research Center of Nano-Geomaterials of Ministry of Education
Faculty of Materials Science and Chemistry
China University of Geosciences
Wuhan 430074, China
E-mail: louxiaoding@cug.edu.cn

Prof. B. Z. Tang
Department of Chemistry
The Hong Kong University of Science and Technology
Clear Water Bay, Kowloon, Hong Kong 999077, China

The ORCID identification number(s) for the author(s) of this article can be found under https://doi.org/10.1002/adma.202101158.

DOI: 10.1002/adma.202101158

be an ideal alternative of preoperative diagnosis and intraoperative navigation to help the surgeon to identify and excise all the tumor nodules as the surgeon's third eyes. Photothermal therapy (PTT) and photodynamic therapy (PDT) are two promising phototherapy modalities, which can effectively convert absorbed light energy with the administration of photosensitizers (PSs) into high local temperature or generate toxic reactive oxygen species (ROS) that kills cancer cell.[8] In addition, by taking advantage of the thermal signal captured by thermal imaging system during PTT, another diagnostic protocol of photothermal imaging (PTI) can be effectively implemented, which can afford possibility for more accurate tumor-imaging cooperated with FLI.[9] As compared to conventional surgery, both of PDT and PTT can offer the merits of convenience, noninvasiveness as well as activation of the antitumor immune system, whereas their antitumor efficacy is usually unsatisfactory to large solid tumor due to the limited light penetration depth.[10] Fortunately, surgery holds the capability of removing large tumor masses and exposing the tumor bed to avoid the critical limitation of phototherapy.[11] Given the circumstances, integrated surgery and phototheranostics for image-guided synergistic cancer therapy are attractive to overcome respective limitations to achieve the maximized therapeutic outcomes and minimized recurrences.

To have the best curative effect as discussion above, the appropriate robust PSs bearing high NIR emission, and photodynamic and photothermal abilities, simultaneously, are of high importance. For constructing multifunctional PSs, the most popular method is to integrate various components with individual specific properties into one platform at present.[12] For instance, Wang and co-workers reported a novel theranostic nanoplatform by combining organic fluorophores (NIR emission and PDT) with inorganic 2D black phosphorus nanosheets (PTT), which performed effectively for image-guided synergistic PDT-PTT phototherapy.[9a] Chen and co-workers combined mitochondria-targeted PS and polydopamine nanoparticles together to realize PDT and PTT functions at the same time for tumor therapy with good efficacy.[13] In spite of its high potential in tumor treatment, this all-in-one method is also limited by the complicated preparation, reduced reproducibility, and indeterminate pharmacokinetics.[14] In this context, in terms of the simpler preparation, defined structure, recognized biocompatibility, and better reproducibility than the all-in-one PSs, multifunctional organic PSs with multiple diagnosis imaging and synergistic therapy functions in one molecule are highly promising and desired for practical and clinical applications.[15] Nevertheless, to the best of our knowledge, such high-quality multifunctional organic PSs with simultaneous NIR FLI, PDT, and PTT have been barely explored.[15,16] In principle, the red/NIR fluorescence needs a narrow bandgap.[17] So, many NIR fluorophores are created into a strong donor–acceptor (D–A) architecture to narrow the bandgap, but the fluorescence efficiency is always exponentially reduced because the excited state returns to the ground state mainly through nonradiative path upon photoexcitation.[18] In other words, the nonradiative decay of excited state can be utilized for PTI and PTT.[4b,19] Based on these considerations, a single PS simultaneously possessing efficient NIR FLI, PDT, and PTT for image-guided synergistic cancer therapy is proposed based on proper molecular design to reasonably modulate radiative and nonradiative pathways of excited state.

In this contribution, we wish to report a novel multifunctional theranostic nanoplatform based on a single luminogenic molecule (DDTB) with aggregation-induced emission (AIE) in near-infrared I/II (NIR-I/II) region (**Scheme 1**). The DDTB-based nanoparticles (DDTB-DP NPs) prepared by encapsulating DDTB within polymeric matrix exhibited remarkable biocompatibility, strong NIR fluorescence peaking at 973 nm, good ROS generation ability and high photothermal conversion efficiency (PCE). Both in vitro and in vivo studies demonstrated that precise NIR FLI image-guided synergistic surgery, PDT, and PTT therapy toward cervical cancer in mice can be achieved under the attendance of the highly versatile DDTB-DP NPs. More importantly, the ingenious theranostic nanoplatform proposed in this work by the integration of conventional surgery and light-dependent PTT and PDT under intraoperative fluorescence navigation can overcome respective limitations for maximally killing the tumor cells and tissues to achieve the maximized therapeutic outcomes and survival rates. Moreover, the tumor immunotherapy combining DDTB-DP NPs mediated PTT/PDT and programmed death-ligand 1 (PD-L1) antibody show significantly improved tumoricidal efficacy to the primary tumor of mice. These studies demonstrated the sophisticated theranostic based on DDTB-DP NPs hold great potential for practical and clinical applications.

2. Result and Discussion

The synthetic route of the designed NIR luminogen DDTB is displayed in Figure S1, Supporting Information, in which the Suzuki coupling of 4,7-dibromobenzo[1,2-c:4,5-c']bis([1,2,5]thiadiazole) (BBTD) and 4,4'-(2-phenyl-2-(4-(4,4,5,5-tetramethyl-1,3,2-dioxaborolan-2-yl)phenyl) ethene-1,1-diyl)bis(*N*,*N*-diphenylaniline) (DDPATPE) using tetrakis(triphenylphosphine)palladium(0) as the catalyst and potassium carbonate as the base in toluene/water yields the target compound. The molecular structure of DDTB is fully characterized by ^{1}H NMR, ^{13}C NMR, and high-resolution mass spectra with satisfactory results (Figures S2–S4, Supporting Information). The detailed experimental procedures and characterization data are described in Supporting Information. DDTB possesses good solubility in common organic solvents, such as chloroform and tetrahydrofuran (THF), while it is insoluble in water.

The optimized molecular conformation and molecular orbital are obtained by density functional theory (DFT) calculation (Figures S5 and S6, Supporting Information). It can be seen that DDTB possesses a highly twisted and branched conformation, which can effectively depress intermolecular π–π stacking. For the electronic structures, the highest occupied molecular orbital (HOMO) is distributed along the entire DDTB molecular skeleton, while the lowest unoccupied molecular orbital (LUMO) is chiefly concentrated on the strong electron-withdrawing BBTD core, indicating that strong intramolecular charge transfer (ICT) can occur in DDTB. The energy bandgap between the HOMO and the LUMO is calculated as

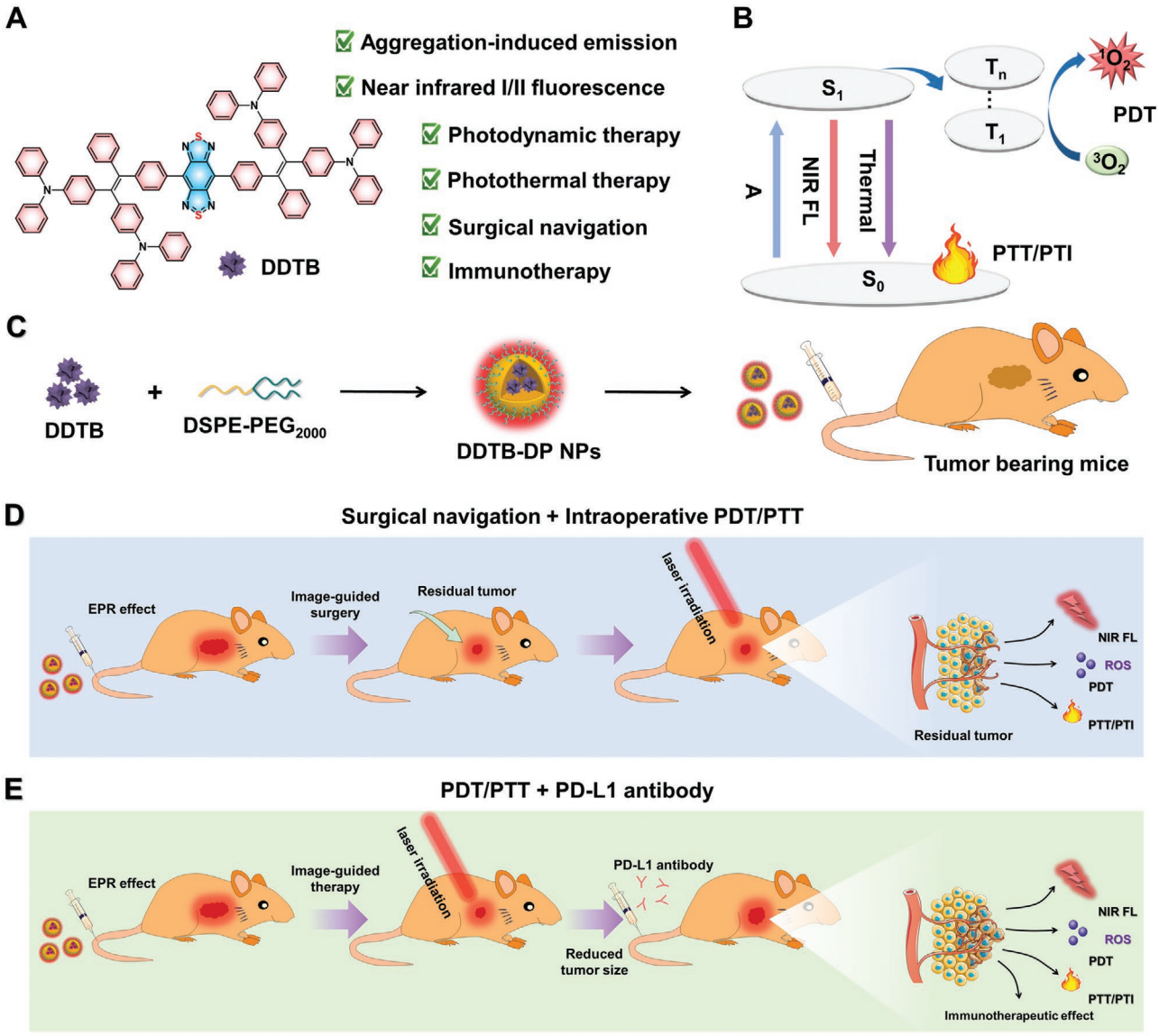

Scheme 1. Schematic illustration of molecular structure, nanofabrication and versatile surgery and phototheranostic application. A) Molecular structure of rationally designed NIR AIEgen DDTB with multifunctional performances. B) Illustration of the reconciled photophysical processes. C) Preparation procedure of DDTB-DP NPs. D,E) Illustrations of the DDTB-DP NPs on NIR FLI image-guided surgery–PTT/PDT (D) and immunotherapy synergistic PTT/PDT tumor treatment (E).

small as 1.38 eV. The strong ICT effect and narrow bandgap will benefit the long-wavelength absorption and emission in the NIR window.

The photophysical property of DDTB is investigated by ultraviolet–visible (UV–vis) absorption and photoluminescence (PL) spectroscopies. As shown in **Figure 1**A, in pure THF solution, DDTB has a strong absorption peak at 650 nm with a high molar absorptivity of 2.17×10^4 M^{-1} cm^{-1} from ICT effect. The fluorescence quantum yield (Φ_F) of DDTB in THF is 0.16%. To investigate the PL behaviors of DDTB in the aggregated state, the PL spectra of DDTB in THF/water mixtures with different water volume fractions (f_w) are monitored (Figure 1B; Figure S7, Supporting Information). By gradually increasing f_w until 30%, the PL signal of DDTB decreases slightly, due to the enhanced ICT effect caused by the increased polarity of the mixture. By further increasing f_w, the PL intensity is increased significantly, which can be explained by the restriction of intramolecular motion (RIM) mechanism. These findings clearly validate the brilliant AIE feature of DDTB.

The low Φ_F of DDTB indicates that the excited state is mainly deactivated via a nonradiative manner. So, it may have good photothermal effect. As expected, it is found that the temperature of DMF solution of DDTB (10^{-4} M) rapidly elevates and reaches up to 91 °C after irradiation with a NIR laser for 3 min (660 nm, 800 mW cm^{-2}) (Figure 1C). This discloses that energy consumption of the excited state is indeed dominated by efficient thermal deactivation pathway through the vigorous intramolecular motions in solution state.

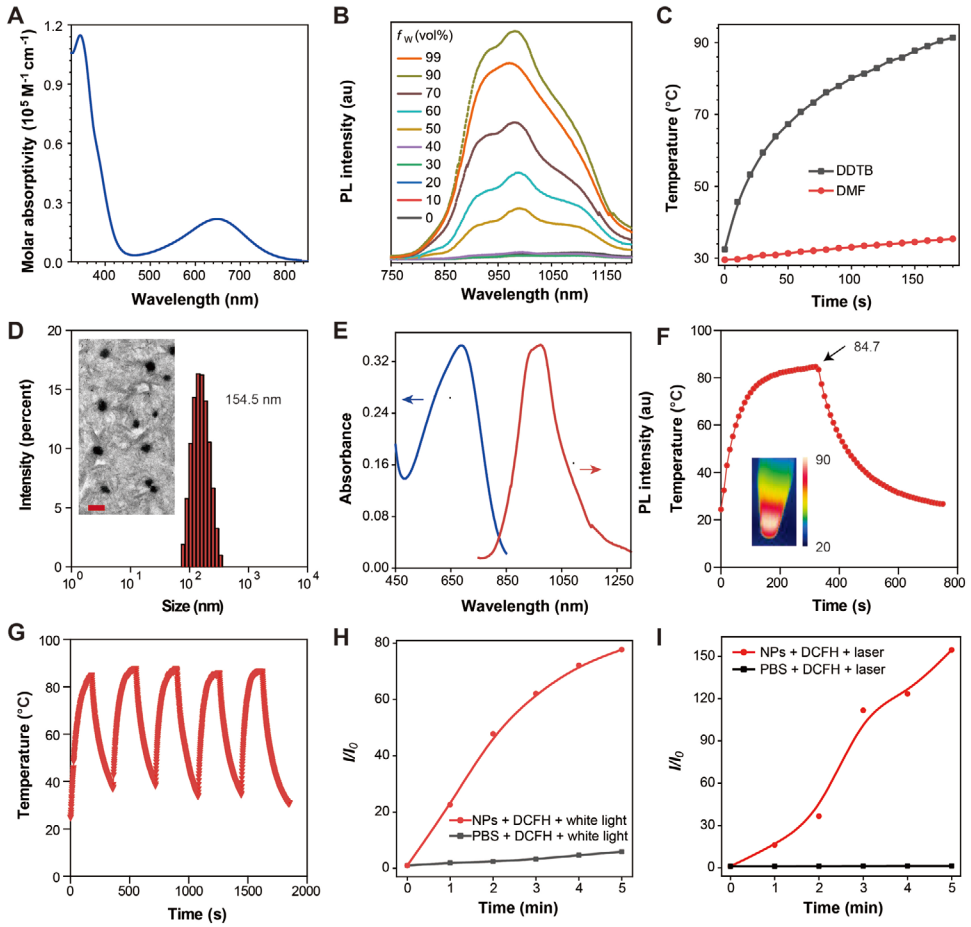

Figure 1. Photophysical, photodynamic, and photothermal properties of DDTB and corresponding NPs. A) UV–vis spectrum of DDTB (10^{-5} M) in THF. B) PL intensity changes of DDTB in THF/water mixtures with different water volume fractions (f_w). C) The photothermal conversion behaviors of DDTB in *N*,*N*-dimethylformamide (DMF) solution under 660 nm laser irradiation (10^{-4} M). D) Dynamic laser scattering size of DDTB-DP NPs and the inset transmission electron microscope image. Scale bar: 200 nm. E) Absorption and emission spectra of the NPs in aqueous solution. F) Temperature elevation of DDTB-DP NPs (10 μg mL^{-1}) in aqueous solution. G) Photothermal stability study of DDTB-DP NPs during five circles of heating–cooling processes. H) Plots of the changes in relative PL intensity of DCFH versus irradiation time in the presence of DDTB-DP NPs (1 μg mL^{-1}) under white-light irradiation (100 mW cm^{-2}). I) Plots of the changes in relative PL intensity of DCFH versus irradiation time in the presence of DDTB-DP NPs (1 μg mL^{-1}) under 660 nm laser irradiation (800 mW cm^{-2}). I_0 and I are the PL intensities of DCFH at 520 nm before and after irradiation, respectively.

Since DDTB is hardly soluble in aqueous medium, to increase water dispersibility as well as biocompatibility, DDTB is processed into nanoparticles (NPs) by using biocompatible encapsulation matrix of 1,2-dis-tearoyl-*sn*-glycero-3-phosphoethanolamine-*N*-[hydroxyl(poly (ethylene glycol))-2000] (DSPE-PEG_{2000}) through common nanoprecipitation method. The obtained DDTB-DP NPs can be well dispersed in aqueous environment with a hydrodynamic diameter of 154.5 nm, as measured by dynamic light scattering (DLS) (Figure 1D). The sphere morphology with an average diameter of 100 nm is observed for DDTB-DP NPs by transmission electron microscopy (TEM). Compared with the DLS result, the smaller size of NPs in TEM image is ascribed to the shrinkage of the NPs in the process of drying TEM samples. According to previous researches, NPs with 10–200 nm diameters can accumulate at tumors due to enhanced permeability and retention (EPR) effect.[20] Thus, the suitable sizes of DDTB-DP NPs should be very helpful for in vivo cancer treatment. Noteworthy, DDTB-DP NPs can be stored for 12 days in phosphate buffer saline (PBS) or 20% fetal bovine serum (FBS) solution at ambient condition without changing the size of NPs, suggesting that DDTB-DP NPs also enjoy great colloidal stability (Figure S8, Supporting Information). As shown in Figure 1E, DDTB-DP NPs have a distinct absorption peak at 687 nm and a wide absorption band from visible to NIR region (480–850 nm). The PL peak of DDTB-DP NPs in aqueous solution is centered at 973 nm, showed a rather large Stokes shift of 286 nm. The Φ_F of DDTB-DP NPs is calculated to be 0.96%, which is higher than the DDTB in molecularly dispersed state. Moreover, almost half of PL spectrum of DDTB-DP NPs is located at the near-infrared II (NIR-II) window (beyond 1000 nm), suggesting that the NPs hold great potential as bright NIR-II FLI probes.

Next, we investigated the photothermal effect of DDTB-DP NPs by NIR laser (660 nm) irradiation in vitro (Figure 1F,G; Figures S9 and S10, Supporting Information). It can be observed that the photothermal effect of the organic NPs is dependent on laser intensity and time as well as NPs' concentration, and thus, the heat generation could be well regulated by these

factors. Notably, the temperature of the DDTB-DP NPs aqueous solution reaches a maximum at 84.7 °C very rapidly after NIR laser irradiation (800 mW cm^{-2}) for 5 min, whereas that of PBS remains almost constant under the same condition. The PCE of these DDTB-DP NPs is determined to be 30.7% by Roper's method, higher than most previously reported photothermal materials including Au nanorods (20.7%), BODIPY derivatives (26.0%) and so forth.[21] It is noteworthy that such NIR NPs enjoy excellent photothermal stability, without decay after five circles of heating–cooling processes, indicating that such nanomaterials hold great potential for repeated or long-term cancer theranostics under NIR laser irradiation. Importantly, the absorption intensity, emission intensity, and hydrodynamic size of DDTB-DP NPs are hardly changed after 660 nm laser irradiation (800 mW cm^{-2}) for 5 min (Figure S11, Supporting Information), indicating that the DDTB-DP NPs possess excellent stability under NIR laser irradiation. More interestingly, the DDTB-DP NPs can also produce ROS during light exposure, as indicated by a universal ROS probe 2,7-dichlorofluorescein (DCFH) because non-fluorescent DCFH can be transformed into green fluorescent 2,7-dichlorodihydrofluorescein (DCF) by the oxidation reaction with ROS. As shown in Figure 1H and Figure S12, Supporting Information, the fluorescence of DCF is rapidly increased in the presence of DDTB-DP NPs under white-light irradiation, while the control group without DDTB-DP NPs shows no obvious fluorescence enhancement. After 5 min irradiation, the fluorescence intensity in the mixture of DDTB-DP NPs and DCFH finally reaches 78-fold enhancement relative to the initial intensity, indicating that the NPs have good ROS generation ability. In addition, 1,3-diphenylisobenzofuran (DPBF) as the $^1O_2$ probe is further used in the experiment to confirm the nature of ROS generated from DDTB-DP NPs (Figure S13, Supporting Information). With white-light irradiation, the absorbance of DPBF in the presence of DDTB-DP NPs decreases rapidly due to the generated $^1O_2$ that decomposes the DPBF, revealing that the ROS produced by DDTB-DP NPs is $^1O_2$. The $^1O_2$ quantum yield of DDTB-DP NPs is measured to be 1.05% (Figures S13 and S14, Supporting Information). In comparison to DDTB in molecularly dispersed solution state, the DDTB-DP NPs have a higher $^1O_2$ generation efficiency (Figure S13C, Supporting Information), implying $^1O_2$ generation benefits from aggregate formation. In addition, DDTB-DP NPs under 660 nm laser irradiation can also produce ROS, and the ROS generation efficiency can be enhanced by strengthening laser power density (Figure 1I; Figures S15 and S16, Supporting Information). Noticeably, the reports about ROS generation of the fluorophores with a BBTD core are very rare.[7c] To understand the ROS generation mechanism of DDTB, time-dependent density functional theory (TD-DFT) calculation is conducted. As shown in Figure S17, Supporting Information, DDTB possesses a small singlet-triplet energy gap (ΔE_{ST}) between low-lying excited singlet and triplet state (S_1/T_2). The small ΔE_{ST} can benefit intersystem crossing (ISC) process from S_1 to T_2, and thus promote efficient conversion of $^3O_2$ to $^1O_2$. However, in molecularly dispersed solution state, the decay of the excited state of DDTB is dominated by thermal deactivation pathway through active intramolecular motion. In NPs state, partial intramolecular motion can be inhibited due to the spatial constraint, which facilitates ISC process from S_1 to T_2 and promotes $^1O_2$ generation. Therefore, DDTB-DP NPs have a higher $^1O_2$ generation efficiency than DDTB-DP in solution state.

To study the cellular uptake of DDTB-DP NPs, cellular imaging is carried out by NIR fluorescence microscopy. After incubation with DDTB-DP NPs for 8 h, NIR fluorescence signal can be successfully detected in HeLa cells under 635 nm excitation (Figure S18, Supporting Information). The CCK-8 assay shows that DDTB-DP NPs without light irradiation have no obvious cytotoxic effect on A549 cells in the concentration range of 0–40 μg mL^{-1}, demonstrating that DDTB-DP NPs hold low dark cytotoxicity (Figure S19, Supporting Information). The NIR laser-induced tumoricidal effects of DDTB-DP NPs toward five different cancer cell lines, A549, MDA-MB-231, SKOV-3, PC-3, and HeLa, are further investigated. As shown in **Figure 2**A, after incubation with DDTB-DP NPs for 8 h, the cancer cells are subject to digestion and centrifugation to obtain cells loaded with the NPs. The temperatures of all the cancer cells loaded with NPs are rapidly increased under irradiation of NIR laser, while that of the cells treated with PBS is nearly unchanged, which are vividly represented by the photos displayed in Figure 2B. In order to intuitively demonstrate the cancer-cell-killing ability of these DDTB-DP NPs, dead cell staining experiment is carried out by employing red fluorescent propidium iodide (PI) as a probe, which can selectively stain dead cells. As expected, red fluorescence is barely observed in the control group upon NIR laser irradiation alone (Figure 2C). By contrast, the groups treated with DDTB-DP NPs and subsequent NIR laser irradiation show bright red fluorescence, apparently demonstrating the strong phototoxicity of DDTB-DP NPs. Similar results can also be observed in Cell Counting Kit-8 (CCK-8) assay (Figure 2D–H). With the increase of DDTB-DP NPs concentration in cells, the cancer cell inhibition becomes more pronounced. When the concentration of DDTB-DP NPs increases to 10 μg mL^{-1}, the enhanced temperature can efficiently cause severe cell death under laser exposure, further confirming the dose-dependent tumoricidal efficacy of NPs with good controllability against A549, MDA-MB-231, SKOV-3, PC-3, and HeLa cells. Moreover, the cellular ROS production performances of DDTB-DP NPs are tested by using 2,7-dichlorofluorescein diacetate (DCFH-DA) as a probe. As illustrated in Figure 2I,J and Figure S20, Supporting Information, the cells treated with DDTB-DP NPs upon white-light irradiation or 660 nm laser irradiation show green fluorescence. In marked contrast, almost no fluorescence can be observed in respective control cells treated with PBS. These results suggest that DDTB-DP NPs as an excellent phototherapy agent is promising candidate for tumor treatment.

Motivated by the outstanding phototheranostic performances of the DDTB-DP NPs in vitro, the DDTB-DP NP-mediated PTT/PDT is explored. First, the tumor imaging effect of DDTB-DP NPs in vivo is investigated on HeLa-tumor-bearing mice to decipher the optimal time point for surgery and phototheranostics. The NIR fluorescence at tumor site with low background interference becomes intense gradually in a time-dependent manner after injection of DDTB-DP NPs into tumor-bearing mice via the tail vein. The fluorescence intensity at tumor site reaches a plateau at 24 h post-injection, implying the sufficient accumulation of the NPs in tumor sites driven by the

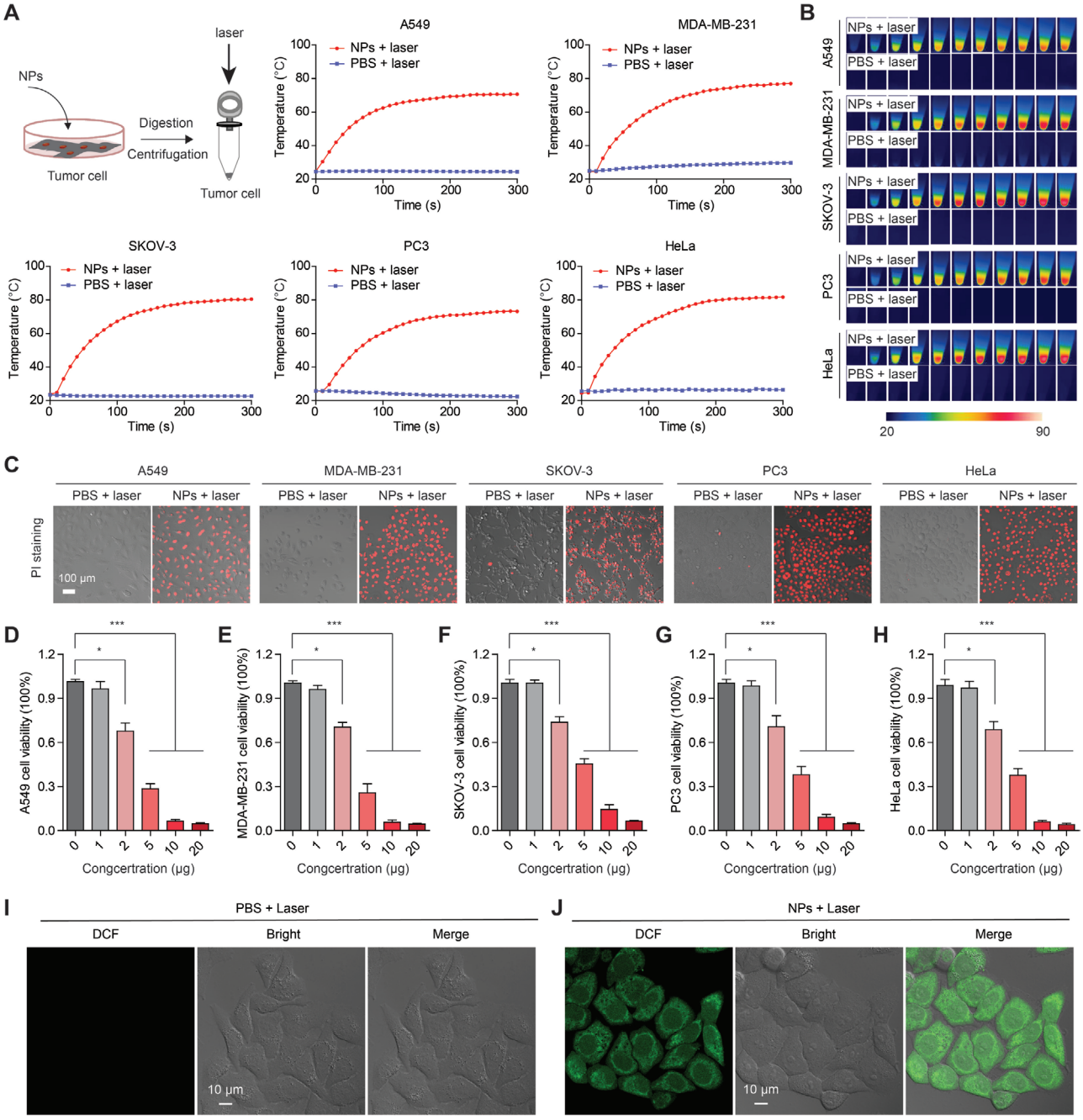

Figure 2. In vitro cell experiments. A) Plots of the changes in temperature of different tumor cells (A549, MDA-MB-231, SKOV-3, PC3 and HeLa) versus irradiation time. B) Infrared thermal images of different tumor cells under 660 nm laser irradiation (800 mW cm^{-2}) after incubation with DDTB-DP NPs and PBS, respectively. C) Dead cell staining assay by using red fluorescent PI to detect the viability of different tumor cells after incubation with NPs for 8 h and treatment with laser irradiation (800 mW cm^{-2}, 5 min). D–H) The CCK-8 assay is conducted to determine the viability of A549 (D), MDA-MB-231 (E), SKOV-3 (F), PC3 (G), and HeLa (H) cells after incubation with different concentrations of NPs for 8 h, respectively, and treatment with laser irradiation (800 mW cm^{-2}, 5 min). I,J) Detection of intracellular ROS generation by DCFH-DA in HeLa cells after incubation without (I) and with (J) DDTB-DP NPs (10 μg mL^{-1}), followed by 660 nm laser irradiation (200 mW cm^{-2}, 5 min). Scale bar: 10 μm. The data are represented as mean ± standard deviation (SD) and analyzed by two-sided Student's *t*-test. $^{*}p < 0.05$, $^{**}p < 0.01$, $^{***}p < 0.001$. n.s., not significant.

EPR effect (**Figure 3**A). Then, tumor resection surgery was conducted, and macroscopic tumors can be removed by the surgeon without fluorescence imaging guidance. However, under NIR fluorescence imaging guidance, we clearly observed two sites with strong fluorescence signals. At this time, secondary surgery guided by NIR fluorescence imaging is performed to excise the two residual tissues with strong fluorescence signals. Thereafter, the mice are sacrificed, and the ex vivo fluorescence signals from the major organs and tumor tissues are detected to study the distribution and metabolism

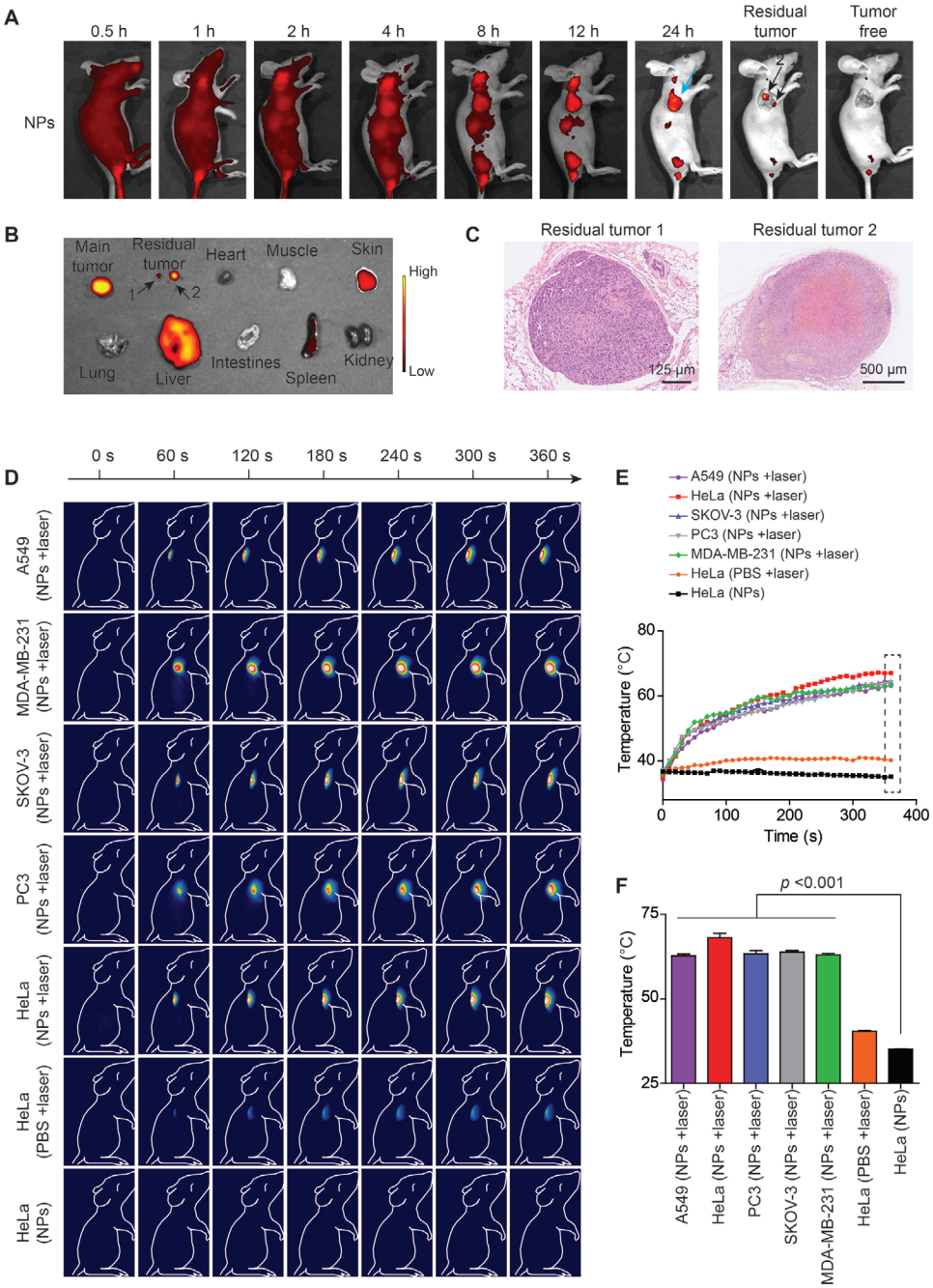

Figure 3. DDTB-DP NPs uptake and photothermal effect in vivo. A) In vivo fluorescence imaging of HeLa-tumor-bearing mice after intravenous injection of DDTB-DP NPs (1 mg mL^{-1}) for different periods of time as indicated. The tumor was removed 24 h after NPs injection, and the residual tumor was removed by secondary surgery guided by fluorescence imaging. B) Representative fluorescence images of the slices of tumor (main tumor and residual tumor) and organs (heart, liver, spleen, lung, and kidneys) resected from the tumor-bearing mice at 24 h post-injection. C) H&E staining of the tiny residual tumor slice. D) Infrared thermal images in the multiple xenograft tumor models under 660 nm laser irradiation (800 mW cm^{-2}) for different treatment times. The laser exposure was performed at 24 h after intravenous injection of 200 μL of DDTB-DP NPs (1 mg mL^{-1}) and PBS. E,F) Temperature changes at the tumor sites as a function of the 660 nm laser (800 mW cm^{-2}) irradiating time, which is the quantitative data of (D). The data are represented as mean ± SD and analyzed by two-sided Student's *t*-test.

of the NPs. It is found that the NPs are mainly accumulated at the tumor sites and liver, followed by the skin and kidney (Figure 3B), according to the intensity of fluorescence signal. In addition, the two removed residual tissues are proven to be tiny tumors by consulting the hematoxylin and eosin (H&E) staining (Figure 3C). These above results indicate that DDTB-DP NPs have remarkable tumor targeting property and long tumor retention stemmed from the EPR effect. Long tumor retention of these NPs is ideal for both preoperative diagnosis and precise tumor resection. Thereupon, the photothermal

effect of DDTB-DP NPs is further evaluated in the following experiments. Five xenograft tumor models of glandular, breast, ovarian, prostate, and cervical tumors are established by using A549, MDA-MB-231, SKOV-3, PC3, and HeLa cells, respectively. After intravenous injection with PBS or DDTB-DP NPs for 24 h, the tumor-bearing mice are treated with or without 660 nm laser irradiation (800 mW cm^{-2}) for 360 s, and then the tumor temperatures are monitored by infrared thermal camera in real time. As illustrated in Figure 3D, in the control groups injected with PBS, the tumor temperatures of the mice treated with irradiation or without irradiation are basically the same. Quite different from the control groups, the tumor temperatures of the group that is injected with the NPs and subject to continuous laser irradiation shows a quick enhancement of about 35 °C, suggesting the promising photothermal conversion capability of DDTB-DP NPs in vivo. Quantitative analysis uncovers that the corresponding temperature during laser irradiation is changed from ≈34 to ≈60 °C, which can cause overheating in tumor tissues adequately (Figure 3E,F).

To better illustrate the in vivo antitumor potency of DDTB-DP NPs, the tumor volumes and mice body weights are continuously monitored for 33 days using three groups of HeLa-tumor-bearing mice (eight mice in each group). Three groups of mice are to undergo different treatments: PBS + Laser, NPs only, and NPs + Laser. The treatment is initiated when the tumors grow to 200 mm^3. As presented in **Figure 4**A,B, the tumors grow fast in the control groups including PBS + laser and NPs only, indicating that neither NPs only nor PBS + laser

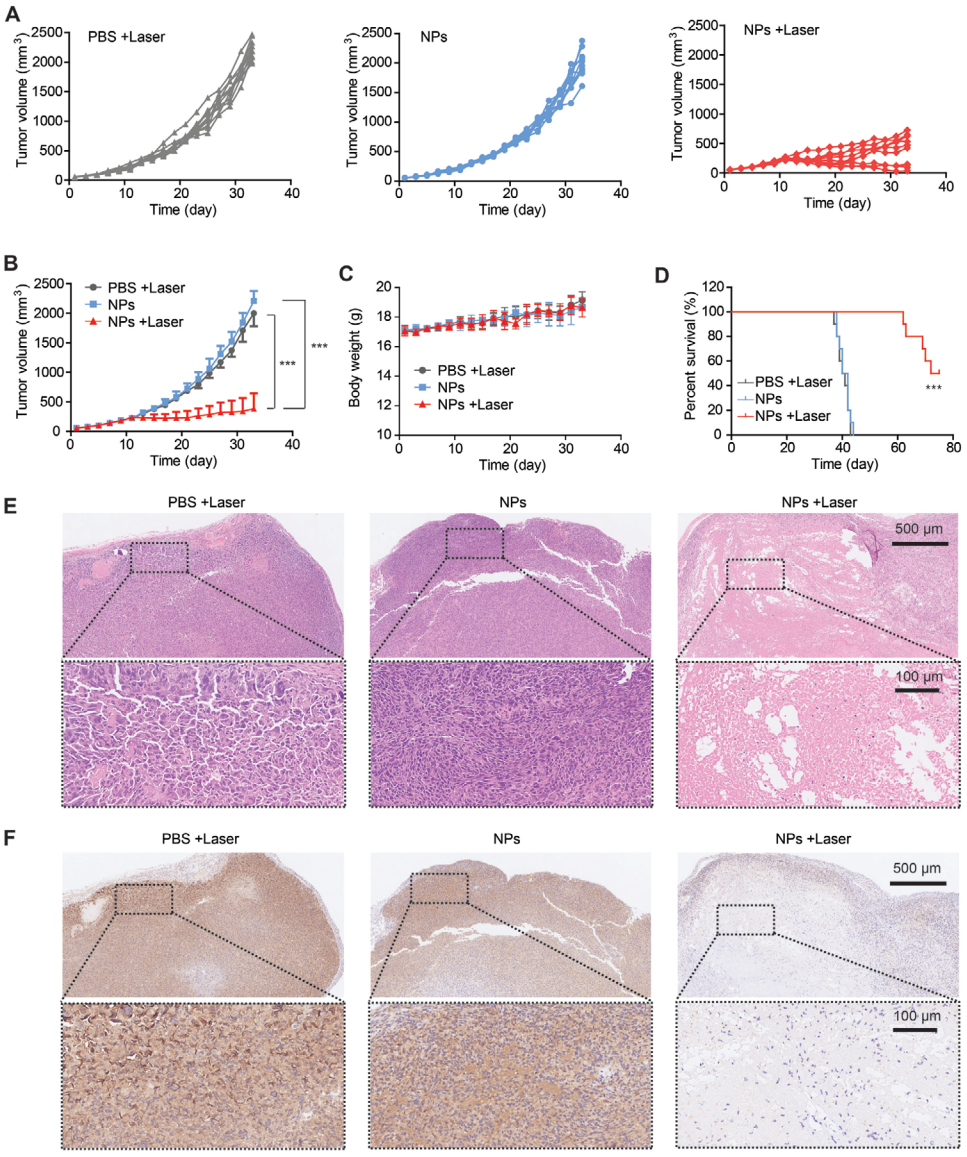

Figure 4. DDTB-DP NPs mediated PTT/PDT for HeLa-tumor-bearing mice. A) Individual and B) average tumor growth curves in different groups. Day 0 indicates the day in which tumors grow to 50 mm^3 in mice. When tumors reach about 200 mm^3, treatment was initiated. Data are presented as mean ± standard error on the mean (s.e.m.) ($n = 8$). C) Body weight of HeLa-tumor-bearing mice in different groups. The data are represented as mean ± SD and analyzed by two-sided Student's *t*-test. ***$p < 0.001$. D) Percentage survival of HeLa-tumor-bearing mice after treatment. The data were analyzed by two-sided log-rank test. ***$p < 0.001$. E) H&E and F) Bcl-2 staining of tumor slices from different treatment groups after treatment.

can generate efficient antitumor activity. In contrast, the tumor volumes are effectively suppressed in NPs + laser group, and even a tumor is completely eliminated. In addition, during the entire treatment period, all the mice in the three groups exhibit normal body weight changes (Figure 4C), manifesting that our treatments do not induce systemic toxic effects to mice. The findings further demonstrate the excellent phototherapy efficacy without side effects of DDTB-DP NPs in vivo and remarkable biosafety as well. It's worth noting that the phototherapy treatment can significantly extend animal survival lifespan (Figure 4D). However, after 60 days, almost half of the mice died, which may be due to the large tumors and limited depth of phototherapy. This may require some adjuvant therapy to improve outcomes.

The H&E and b-cell lymphoma-2 (Bcl-2) staining of tumor slices from different treatment groups are further examined at autopsy to help unveil the antitumor mechanism of DDTB-DP NPs. Figure 4E shows severe apoptosis and necrosis in the NPs + laser group, whereas in the other groups of PBS + laser and NPs only the cancer cells are closely aligned without obvious damage. The significant low expression of Bcl-2, an anti-apoptotic gene, can be observed in the NPs + laser group, while high expressions of Bcl-2 are found in PBS + laser and NPs only groups (Figure 4F). These results reveal that NIR laser-induced local hyperthermia based on DDTB-DP NPs can severely destruct tumor tissues, and inhibit the expression of Bcl-2 to promote apoptosis, thereby depressing the tumor growth effectively. More importantly, no appreciable damage is observed in major organs of mice including heart, kidney, spleen, liver, and lung from different treatment groups, manifesting once again the remarkable biosafety of DDTB-DP NPs (Figure S21, Supporting Information).

In the clinic, local recurrence due to the tiny residual tumors left behind post-major tumor excision during surgery is a main cause of treatment failure for patients. It is of high significance to sensitively detect and visualize the residual tumors as the surgeon's third eyes for precise and thorough elimination of tumor. Although PTT and PDT have been recognized as general phototherapy protocols for tumor treatment, limited penetration depth of light, therapeutic outcomes may also be diluted. To further prolong animal survival and reduce cancer recurrence as much as possible, a multimodal tumor treatment protocol by integrating PTT and PDT with fluorescence-image-guided surgery is proposed. The schematic illustration of image-guided surgery–PTT/PDT is shown in **Figure 5**A. The bioluminescent HeLa-tumor-bearing mice models are established by using enhanced green fluorescent protein (EGFP)-expressed HeLa tumor cells, allowing for precise assessment of tumor recurrence after treatment. The HeLa-tumor-bearing mice are randomly divided into four groups ($n = 10$) using different treatment strategies: Con group (the mice received no surgical treatment as the control), Surg group (surgery without image-guidance), I-surg (image-guided surgery) group, and I-surg–PTT/PDT group (image-guided surgery and intraoperative photodynamic and photothermal therapy). Tumor growth is monitored by means of using both in vivo bioluminescence (Figure 5B) and caliper measurement (Figure 5C,D). In Con group, the tumor grows crazy as the time elapsed, and all tumor-bearing mice still keep tumor. Thus, we define a tumor recurrence rate of 100% for this control group. On the contrary, because of the tumor excision by various treatments, the tumor volumes are significantly decreased at 25 days in the Surg, I-surg, and I-surg–PTT/PDT groups. However, after treatments, the tumors from 8 of 10 mice in the Surg group and 5 of 10 mice in the I-Surg group are greatly increased with obvious recurrence. The I-Surg group shows lower recurrence rate compared with the Surg group, which should be benefited from the third eye of surgeon to distinguish more tiny residual tumor tissues. Noteworthy, only 1 of 10 mice in the I-surg–PTT/PDT group has relapsed tumor, verifying the satisfactory therapeutic effect of I-surg–PTT/PDT treatment. According to the results illustrated in Figure 5B–D, the tendency of tumor recurrence is Con (100%) > Surg (80%) > I-surg (50%) > I-surg–PTT/PDT (10%) (Figure 5E). In the I-surg–PTT/PDT group, the median overall survival (OS) of treated mice is greater than 70 days, which is determined to be much greater than the median OS in the other groups (Figure 5F). The aforementioned results have reasonably demonstrated that the synergistic image-guided surgery–PTT/PDT hold a better therapeutic outcome than other therapeutic methods. The new multimodal therapy protocol proposed in this work by the combination of conventional surgery and light-dependent PTT/PDT under the guidance of NIR fluorescence imaging can overcome respective limitations, rendering great promise for clinical application.

In recent years, tumor immunotherapy has brought great potential to fight against cancer. In view of this, we finally evaluate whether these NPs plus PD-L1 antibody upon the light irradiation can improve the antitumor immune system in primary tumor of mice for modern tumor immunotherapy. The PD-L1 is an important immune checkpoint, leading to inhibition of T cell activation, which can be suppressed by PD-L1 antibody that will reactivate the immune response of T cells to tumor cells to achieve antitumor effect.[22] Two xenograft tumor models of melanoma and breast tumors are established by using B16-F10 and 4T1 tumor cells, respectively. The treatments are carried out at 24 h post-intravenous injection. According to the tumor photographs (**Figure 6**A,D) and tumor growth curves (Figure 6B,E), NPs + laser and PD-L1 antibody alone groups could effectively inhibit the development of tumor growth in two tumors compared to PBS and NPs groups. Unexpectedly, NPs + laser plus PD-L1 antibody exhibits the best antitumor potency, and most tumors are ablated without any recurrence, disclosing that the combined treatment of DDTB-DP NPs-mediated PTT/PDT and PD-L1 antibody can enhance the therapeutic effect. Additionally, none of the mice show significant weight loss for all groups (Figure 6C,F). The significantly improved tumor immunotherapy by the combination of PTT/PDT and PD-L1 antibody is further confirmed by flow cytometry and immunofluorescence imaging (Figure 6G–K; Figure S22, Supporting Information). Obviously, as compared with those in all other groups, cytotoxic $CD4^+$, and $CD8^+$ T lymphocytes that are responsible for antitumor immunity display significant increase in the NPs + laser + anti-PD-L1 group. Moreover, it is found that the concentrations of multiple cytokines like tumor necrosis factor-α (TNF-α) and interferon-γ (IFN-γ) released by T cells in peripheral blood of tumor-bearing mice are also remarkably enhanced, especially in the mice treated with the DDTB-DP NPs-mediated PTT/PDT plus PD-L1

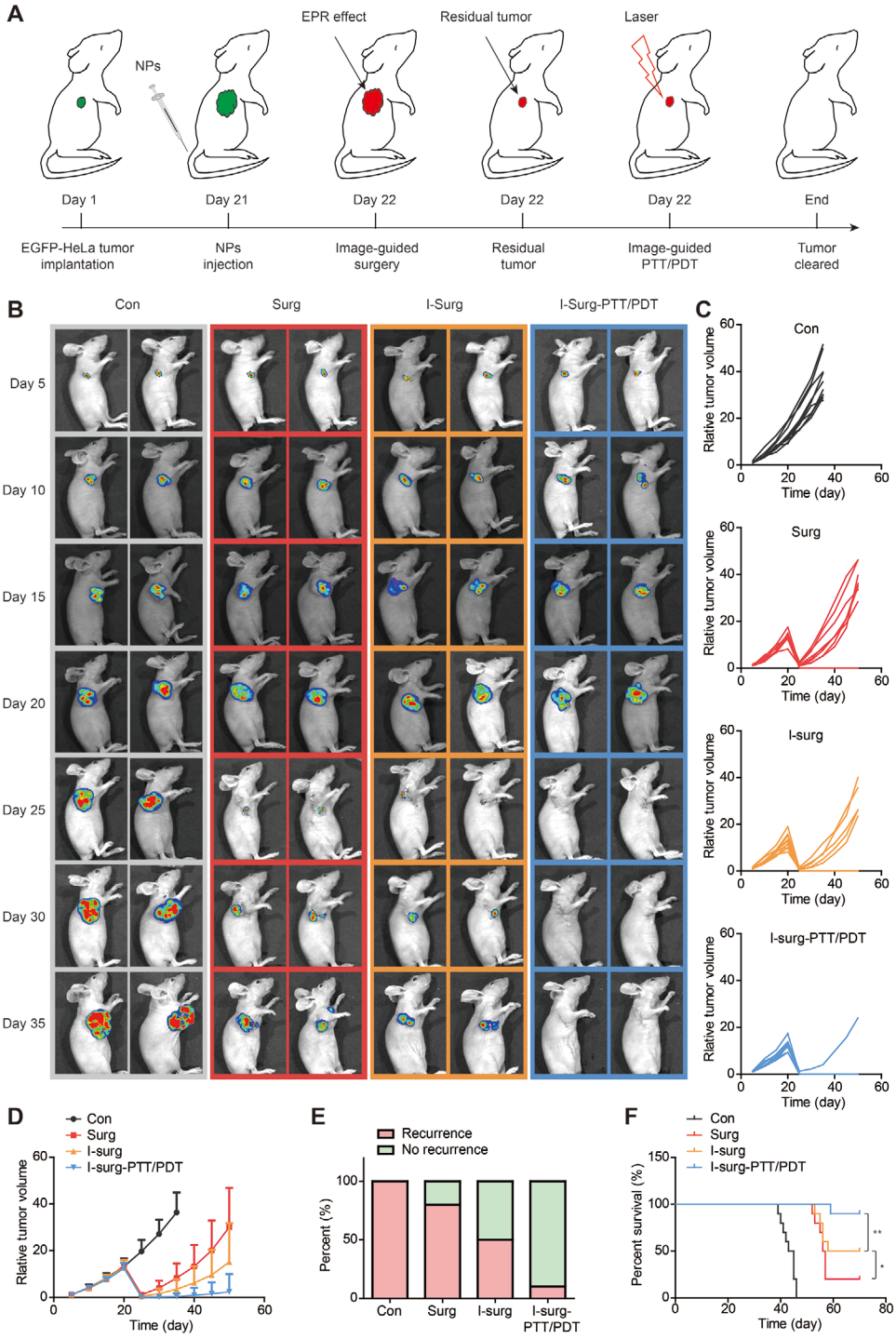

Figure 5. In vivo image-guided synergistic therapeutic efficiency of DDTB-DP NPs on EGFP-HeLa-tumor-bearing mice through systemic administration. A) Schematic illustration of image-guided surgery–PTT/PDT to tumors. B) Representative bioluminescence images were performed to monitor tumor recurrence after the treatment in all mice. C) Individual and D) average tumor growth curves of HeLa-tumor-bearing mice from different groups of mice ($n = 10$ per group). E) Tumor recurrence rate of different groups after treatment. F) Survival curves of different groups after treatment. The data were analyzed by two-sided log-rank test. $^{*}p < 0.05$, $^{**}p < 0.01$.

antibody treatment. This is because the hyperthermia in tumor caused by strong and efficient PTT can increase vascular permeability, which is conducive to enhancing PD-L1 antibody infiltration efficiency.[23] Moreover, the accumulation of $CD4^+$ and $CD8^+$ T lymphocytes in tumor is increased, which is most apparent in NPs + laser + anti-PD-L1 group (Figure 6K). These results further reveal that the combination of DDTB-DP NPs-mediated PTT/PDT and PD-L1 antibody effectively induces

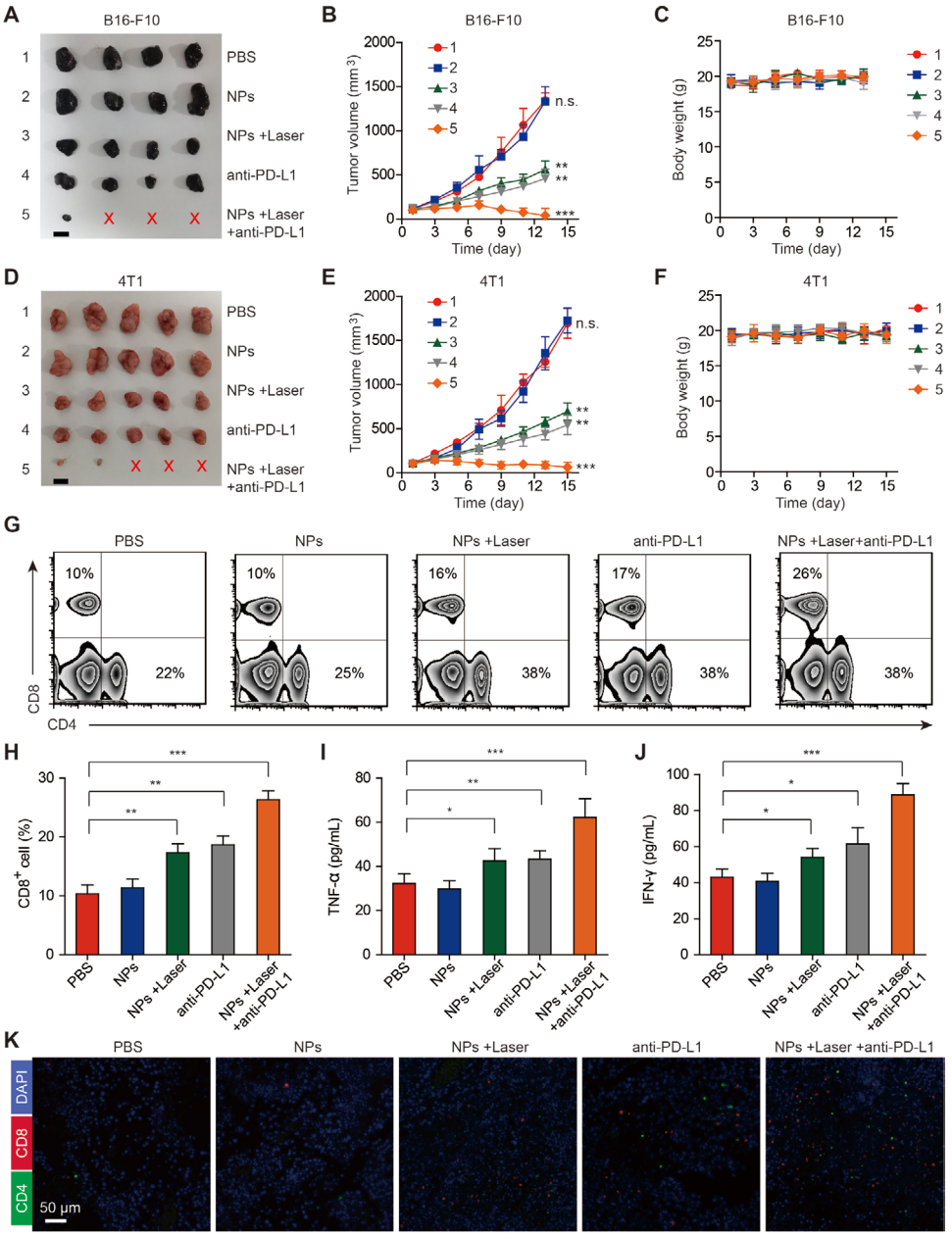

Figure 6. Tumor immunotherapy combining DDTB-DP NPs mediated PTT/PDT and PD-L1 antibody. A) Representative tumor images of B16-F10-tumor-bearing mice after treatment, the red X indicates no tumor was detected. B) Tumor volume growth curves of B16-F10-tumor-bearing mice at different times after treatment. C) Body-weight measurements of B16-F10-tumor-bearing mice in different groups. D) Representative tumor images of 4T1-tumor-bearing mice after treatment. E) Tumor volume growth curves of 4T1-tumor-bearing mice at different times after treatment. F) Body weight measurements of 4T1-tumor-bearing mice in different groups. G) The representative flow cytometric plots of $CD8^+$ T cell in T cell for peripheral blood of mice from various groups. H) Proportions of $CD8^+$ T cells in peripheral blood. I) TNF-α secretion and J) IFN-γ secretion in peripheral blood. K) Representative immunofluorescence of tumors showing that $CD4^+$ and $CD8^+$ T cells infiltrating the tumor from various groups. The data are represented as mean ± SD and were analyzed by two-sided Student's *t*-test. $P < 0.05$, $^{**}p < 0.01$, $^{***}p < 0.001$, n.s., not significant.

the antitumor immune system to achieve satisfactory tumor immunotherapy.

3. Conclusion

Robust multifunctional fluorescent reagent plays a key role in the successful implementation of multimodal image-guided synergistic tumor treatment. In this work, we designed and synthesized a multifunctional fluorophore DDTB comprised of an electron-withdrawing BBTD core and electron-donating DDPATPE functional groups. DDTB displays obvious AIE property, due to the presence of many rotatable phenyl rotors, and affords NIR fluorescence originating from the strong ICT effect and a narrow bandgap. The partial excited state energy of DDTB under photoexcitation is dissipated in a nonradiative manner,

which endows DDTB with excellent photothermal performance. In addition, DDTB possesses good ROS generation ability benefitting from a low-lying S_1, which enables ISC process of $S_1 \rightarrow T_2$ and thus facilitates the conversion of $^3O_2 \rightarrow {}^1O_2$. In the aggregated state, the ISC process can be prompted, leading to a higher $^1O_2$ generation efficiency than in the solution state. It is envisioned that, the introduction of other photophysical mechanisms, such as delayed fluorescence, room-temperature phosphorescence, heavy-atom effect, and radical or magnetic property, as well as specific substituents, such as stimulus-responsive, targeting and medicative groups, may bring about new functionalities for AIEgens for biomedical applications.

Based on the intriguing functions of DDTB, versatile DDTB-DP NPs are formulated by encapsulating DDTB within polymeric matrix (DSPE-PEG_{2000}) for tumor diagnosis and therapy. Our in vitro studies reveal that these DDTB-DP NPs holds high water-stability, strong NIR fluorescence at ≈973 nm, effective ROS generation and high PCE of 30.7%. In vivo experiments strongly announce that the DDTB-DP NP with desirable biocompatibility and biosafety well accomplished in pre/intraoperative NIR FLI image-guided synergistic surgery–PTT/PDT tumor treatment, improving the therapeutic efficacy for maximizing the survival of mice. On the other hand, the tumor immunotherapy combining DDTB-DP NPs-mediated PTT/PDT and PD-L1 antibody can significantly improve the antitumor immune system in primary tumor of mice. The advantages of AIEgens in nanoparticle state, such as strong NIR emission, high photostability, and excellent phototherapy ability, could be further integrated with other clinical diagnostic imaging and treatment techniques to realize more precise and specific theranostics for clinical application.

Supporting Information

Supporting Information is available from the Wiley Online Library or from the author.

Acknowledgements

R.J. and J.D. contributed equally to this work. The authors thank the financial support from the National Natural Science Foundation of China (21788102, 21874121, and 21974128) and the Natural Science Foundation of Guangdong Province (2019B030301003).

Conflict of Interest

The authors declare no conflict of interest.

Data Availability Statement

Research data are not shared.

Keywords

aggregation-induced emission, immunotherapy, intraoperative fluorescence navigation, multimodal therapy, phototheranostics

Received: February 9, 2021
Revised: March 7, 2021
Published online:

[1] a) Y. Wang, N. Gong, Y. Li, Q. Lu, X. Wang, J. Li, *J. Am. Chem. Soc.* **2020**, *142*, 1735; b) B. Guo, Z. Huang, Q. Shi, E. Middha, S. Xu, L. Li, M. Wu, J. Jiang, Q. Hu, Z. Fu, B. Liu, *Adv. Funct. Mater.* **2020**, *30*, 1907093; c) K. Chang, Y. Liu, D. Hu, Q. Qi, D. Gao, Y. Wang, D. Li, X. Zhang, H. Zheng, Z. Sheng, Z. Yuan, *ACS Appl. Mater. Interfaces* **2018**, *10*, 7012; d) M. Jiang, R. T. K. Kwok, X. Li, C. Gui, J. W. Y. Lam, J. Qu, B. Z. Tang, *J. Mater. Chem. B* **2018**, *6*, 2557; e) M. J. Friedrich, *JAMA, J. Am. Med. Assoc.* **2019**, *321*, 1041.

[2] a) J. Dai, Y. Cheng, J. Wu, Q. Wang, W. Wang, J. Yang, Z. Zhao, X. Lou, F. Xia, S. Wang, B. Z. Tang, *ACS Nano* **2020**, *14*, 14698; b) Q. Chen, C. Liang, X. Wang, J. He, Y. Li, Z. Liu, *Biomaterials* **2014**, *35*, 9355; c) J. Dai, M. Xu, Q. Wang, J. Yang, J. Zhang, P. Cui, W. Wang, X. Lou, F. Xia, S. Wang, *Theranostics* **2020**, *10*, 2385.

[3] a) P. Wang, Y. Fan, L. Lu, L. Liu, L. Fan, M. Zhao, Y. Xie, C. Xu, F. Zhang, *Nat. Commun.* **2018**, *9*, 2898; b) X. Wang, G. Ramamurthy, A. Shirke, E. Walker, J. Mangadlao, Z. Wang, Y. Wang, L. Shan, M. Schluchter, Z. Dong, S. M. Brady-Kalnay, N. K. Walker, M. Gargesha, G. MacLennan, D. Luo, R. Sun, B. Scott, D. Roy, J. Li, J. P. Basilion, *Cancer Res.* **2020**, *80*, 156; c) N. Muhanna, L. Cui, H. Chan, L. Burgess, C. S. Jin, T. D. MacDonald, E. Huynh, F. Wang, J. Chen, J. C. Irish, G. Zheng, *Clin. Cancer Res.* **2016**, *22*, 961; d) P. Debie, N. Devoogdt, S. Hernot, *Antibodies* **2019**, *8*, 12.

[4] a) J. Zou, J. Zhu, Z. Yang, L. Li, W. Fan, L. He, W. Tang, L. Deng, J. Mu, Y. Ma, Y. Cheng, W. Huang, X. Dong, X. Chen, *Angew. Chem., Int. Ed.* **2020**, *59*, 8833; b) Q. Wan, R. Zhang, Z. Zhuang, Y. Li, Y. Huang, Z. Wang, W. Zhang, J. Hou, B. Z. Tang, *Adv. Funct. Mater.* **2020**, *30*, 2002057; c) Y. Zi-Shu, Y. Yuhang, A. C. Sedgwick, L. Cuicui, X. Ye, W. Yan, K. Lei, S. Hongmei, W. Bing-Wu, G. Song, *Chem. Sci.* **2020**, *11*, 8204; d) Y. Niu, G. Ling, L. Wang, S. Guan, Z. Xie, E. A. Barnoy, S. Zhou, D. Fixler, *Nanomaterials* **2018**, *8*, 706; e) H. Xu, Y. Han, G. Zhao, L. Zhang, Z. Zhao, Z. Wang, L. Zhao, L. Hua, K. Naveena, J. Lu, R. Yu, H. Liu, *ACS Appl. Mater. Interfaces* **2020**, *12*, 52319.

[5] a) Z. Yang, Y. Du, Q. Sun, Y. Peng, R. Wang, Y. Zhou, Y. Wang, C. Zhang, X. Qi, *ACS Nano* **2020**, *14*, 6191; b) J. Song, N. Zhang, L. Zhang, H. Yi, Y. Liu, Y. Li, X. Li, M. Wu, L. Hao, Z. Yang, Z. Wang, *Int. J. Nanomed.* **2019**, *14*, 2757; c) Y. Ju, B. Dong, J. Yu, Y. Hou, *Nano Today* **2019**, *26*, 108.

[6] a) S. Liu, C. Chen, Y. Li, H. Zhang, J. Liu, R. Wang, S. T. H. Wong, J. W. Y. Lam, D. Ding, B. Z. Tang, *Adv. Funct. Mater.* **2020**, *30*, 1908125; b) J. Qi, X. Duan, W. Liu, Y. Li, Y. Cai, J. W. Y. Lam, R. T. K. Kwoka, D. Ding, B. Z. Tang, *Biomaterials* **2020**, *248*, 120036; c) Y. Cheng, J. Dai, C. Sun, R. Liu, T. Zhai, X. Lou, F. Xia, *Angew. Chem., Int. Ed.* **2018**, *57*, 3123; d) J. Yang, J. Dai, Q. Wang, Y. Cheng, J. Guo, Z. Zhao, Y. Hong, X. Lou, F. Xia, *Angew. Chem., Int. Ed.* **2020**, *59*, 20405.

[7] a) Q. Wen, Y. Zhang, C. Li, S. Ling, X. Yang, G. Chen, Y. Yang, Q. Wang, *Angew. Chem., Int. Ed.* **2019**, *58*, 11001; b) Y. Yang, X. Fan, L. Li, Y. Yang, A. Nuernisha, D. Xue, C. He, J. Qian, Q. Hu, H. Chen, J. Liu, W. Huang, *ACS Nano* **2020**, *14*, 2509; c) S. Gao, G. Wei, S. Zhang, B. Zheng, J. Xu, G. Chen, M. Li, S. Song, W. Fu, Z. Xiao, W. Lu, *Nat. Commun.* **2019**, *10*, 2206.

[8] a) Y. Dai, J. Su, K. Wu, W. Ma, B. Wang, M. Li, P. Sung, Q. Shen, Q. Wang, Q. Fan, *ACS Appl. Mater. Interfaces* **2019**, *11*, 10540; b) Z. Long, J. Dai, Q. Hu, Q. Wang, S. Zhen, Z. Zhao, Z. Liu, J. Hu, X. Lou, F. Xia, *Theranostics* **2020**, *10*, 2260; c) Z. Zhuang, J. Dai, M. Yu, J. Li, P. Shen, R. Hu, X. Lou, Z. Zhao, B. Z. Tang, *Chem. Sci.* **2020**, *11*, 3405; d) J. Mou, T. Lin, F. Huang, H. Chen, J. Shi, *Biomaterials* **2016**, *84*, 13; e) C. Chen, X. Ni, S. Jia, Y. Liang, X. Wu, D. Kong, D. Ding, *Adv. Mater.* **2019**, *31*, 1904914; f) H. Yao, J. Dai, Z. Zhuang, J. Yao, Z. Wu, S. Wang, F. Xia, J. Zhou, X. Lou, Z. Zhao, *Sci. China Chem.* **2020**, *63*, 12.

[9] a) J. Huang, B. He, Z. Zhang, Y. Li, M. Kang, Y. Wang, K. Li, D. Wang, B. Z. Tang, *Adv. Mater.* **2020**, *32*, 2003382; b) Y. Xiao,

F. An, J. Chen, J. Yu, W. Tao, Z. Yu, R. Ting, C. Lee, X. Zhang, *Small* **2019**, *15*, 1903121.

[10] a) J. Song, L. Zhang, H. Yi, J. Huang, N. Zhang, Y. Zhong, L. Hao, K. Yang, Z. Wang, D. Wang, Z. Yang, *Nanomed. Nanotechnol.* **2019**, *20*, 102020; b) J. Hu, W. Jiang, L. Yuan, C. Duan, Q. Yuan, Z. Long, X. Lou, F. Xia, *Aggregate* **2021**, *2*, 48; c) J. Qi, H. Ou, Q. Liu, D. Ding, *Aggregate* **2021**, *2*, 95.

[11] C. Chen, X. Ni, H. Tian, Q. Liu, D. Guo, D. Ding, *Angew. Chem., Int. Ed.* **2020**, *59*, 10008.

[12] Q. Wang, Y. Dai, J. Xu, J. Cai, X. Niu, L. Zhang, R. Chen, Q. Shen, W. Huang, Q. Fan, *Adv. Funct. Mater.* **2019**, *29*, 1901480.

[13] Y. Chen, W. Ai, X. Guo, Y. Li, Y. Ma, L. Chen, H. Zhang, T. Wang, X. Zhang, Z. Wang, *Small* **2019**, *15*, 1902352.

[14] J. Qi, J. Li, R. Liu, Q. Li, H. Zhang, J. W. Y. Lam, R. T. K. Kwok, D. Liu, D. Ding, B. Z. Tang, *Chem* **2019**, *5*, 2657.

[15] Z. Zhang, W. Xu, M. Kang, H. Wen, H. Guo, P. Zhang, L. Xi, K. Li, L. Wang, D. Wang, B. Z. Tang, *Adv. Mater.* **2020**, *32*, 2003210.

[16] a) W. Xu, Z. Zhang, M. Kang, H. Guo, Y. Li, H. Wen, M. M. S. Lee, Z. Wang, R. T. K. Kwok, J. W. Y. Lam, K. Li, L. Xi, S. Chen, D. Wang, B. Z. Tang, *ACS Mater. Lett.* **2020**, *2*, 1033; b) X. Liu, Y. Duan, B. Liu, *Aggregate* **2021**, *2*, 4; c) D. Mao, W. Wu, S. Ji, C. Chen, F. Hu, D. Kong, D. Ding, B. Liu, *Chem* **2017**, *3*, 991; d) J. Geng, C. Sun, J. Liu, L. Liao, Y. Yuan, N. Thakor, J. Wang, B. Liu, *Small* **2015**, *11*, 1603.

[17] a) X. Han, Q. Bai, L. Yao, H. Liu, Y. Gao, J. Li, L. Liu, Y. Liu, X. Li, P. Lu, B. Yang, *Adv. Funct. Mater.* **2015**, *25*, 7521; b) G. Qian, Z. Zhong, M. Luo, D. Yu, Z. Zhang, Z. Y. Wang, D. Ma, *Adv. Mater.* **2009**, *21*, 111; c) Q. Xia, Z. Chen, Z. Yu, L. Wang, J. Qu, R. Liu, *ACS Appl. Mater. Interfaces* **2018**, *10*, 17081.

[18] a) S. Liu, X. Zhou, H. Zhang, H. Ou, J. W. Y. Lam, Y. Liu, L. Shi, D. Ding, B. Z. Tang, *J. Am. Chem. Soc.* **2019**, *141*, 5359; b) D. Xi, M. Xiao, J. Cao, L. Zhao, N. Xu, S. Long, J. Fan, K. Shao, W. Sun, X. Yan, X. Peng, *Adv. Mater.* **2020**, *32*, 1907855; c) S. Zhen, S. Wang, S. Li, W. Luo, M. Gao, L. G. Ng, C. C. Goh, A. Qin, Z. Zhao, B. Liu, B. Z. Tang, *Adv. Funct. Mater.* **2018**, *28*, 1706945.

[19] a) J. Dai, Y. Li, Z. Long, R. Jiang, Z. Zhuang, Z. Wang, Z. Zhao, X. Lou, F. Xia, B. Z. Tang, *ACS Nano* **2020**, *14*, 854; b) H. Gao, X. Zhao, S. Chen, *Molecules* **2018**, *23*, 419; c) J. Mei, N. L. C. Leung, R. T. K. Kwok, J. W. Y. Lam, B. Z. Tang, *Chem. Rev.* **2015**, *115*, 11718; d) J. Mei, Y. Hong, J. W. Y. Lam, A. Qin, Y. Tang, B. Z. Tang, *Adv. Mater.* **2014**, *26*, 5429.

[20] L. Cui, Q. Lin, C. S. Jin, W. Jiang, H. Huang, L. Ding, N. Muhanna, J. C. Irish, F. Wang, J. Chen, G. Zheng, *ACS Nano* **2015**, *9*, 4484.

[21] a) L. Luo, Y. Bian, Y. Liu, X. Zhang, M. Wang, S. Xing, L. Li, D. Gao, *Small* **2016**, *12*, 4103; b) S. Ye, J. Rao, S. Qiu, J. Zhao, H. He, Z. Yan, T. Yang, Y. Deng, H. Ke, H. Yang, Y. Zhao, Z. Guo, H. Chen, *Adv. Mater.* **2018**, *30*, 1801216; c) Z. Zhao, C. Chen, W. Wu, F. Wang, L. Du, X. Zhang, Y. Xiong, X. He, Y. Cai, R. T. K. Kwok, J. W. Y. Lam, X. Gao, P. Sun, D. L. Phillips, D. Ding, B. Z. Tang, *Nat. Commun.* **2019**, *10*, 768.

[22] a) S. L. Topalian, J. M. Taube, D. M. Pardoll, *Science* **2020**, *367*, eaax0182; b) X. Liu, J. Zheng, W. Sun, X. Zhao, Y. Li, N. Gong, Y. Wang, X. Ma, T. Zhang, L. Zhao, Y. Hou, Z. Wu, Y. Du, H. Fan, J. Tian, X. Liang, *ACS Nano* **2019**, *13*, 8811; c) Y. Li, R. Zhao, K. Cheng, K. Zhang, Y. Wang, Y. Zhang, Y. Li, G. Liu, J. Xu, J. Xu, G. J. Anderson, J. Shi, L. Ren, X. Zhao, G. Nie, *ACS Nano* **2020**, *14*, 16698.

[23] a) S. Clement, J. M. Campbell, W. Deng, A. Guller, S. Nisar, G. Liu, B. C. Wilson, E. M. Goldys, *Adv. Sci.* **2020**, *7*, 2003584; b) A. P. Castano, P. Mroz, M. R. Hamblin, *Nat. Rev. Cancer* **2006**, *6*, 535; c) J. Dai, M. Wu, Q. Wang, S. Ding, X. Dong, L. Xue, Q. Zhu, J. Zhou, F. Xia, S. Wang, Y. Hong, *Natl. Sci. Rev.* **2021**, *8*, nwab039; d) Q. Chen, Q. Hu, E. Dukhovlinova, G. Chen, S. Ahn, C. Wang, E. A. Ogunnaike, F. S. Ligler, G. Dotti, Z. Gu, *Adv. Mater.* **2019**, *31*, 1900192.